

## Towards a high-intensity muon source

Han-Jie Cai<sup>1,2</sup>, Yuan He<sup>1,2,\*</sup>, Shuhui Liu<sup>1,2</sup>, Huan Jia<sup>1,2</sup>, Yuanshuai Qin<sup>1</sup>, Zhijun Wang<sup>1,2</sup>, Fengfeng Wang<sup>1,2</sup>, Lixia Zhao<sup>1</sup>, Neng Pu<sup>1</sup>, Jianwei Niu<sup>1,2,3</sup>, Liangwen Chen<sup>1,2</sup>, Zhiyu Sun<sup>1,2</sup>, Hongwei Zhao<sup>1,2</sup> and Wenlong Zhan<sup>1,2,4</sup>

<sup>1</sup>*Institute of Modern Physics, Chinese Academy of Sciences, Lanzhou 730000, China*

<sup>2</sup>*School of Nuclear Science and Technology, University of the Chinese Academy of Sciences, Beijing 100049, China*

<sup>3</sup>*Lanzhou University, Lanzhou 730000, China*

<sup>4</sup>*Chinese Academy of Sciences, Beijing 100864, China*

 (Received 4 September 2023; accepted 12 February 2024; published 27 February 2024)

A high-intensity muon source driven by a continuous-wave superconducting linac holds the potential to significantly advance the intensity frontier of muon sources. Alongside advancements in accelerator technologies, breakthroughs in muon production target and collection schemes are essential. After a brief introduction to the development of the accelerator-driven system superconducting linac, a novel muon production target is proposed, utilizing a free-surface liquid lithium jet capable of handling the heat power generated by a proton beam with an energy of 600 MeV and a current of 5 mA. It is predicted by our simulation studies that the lithium target is more efficient in surface muon production compared to the rotating graphite target. The parameter space of the front end consisting of a lithium target and a large-aperture capture solenoid is explored, from the perspective of production efficiency, capture efficiency, and characteristics of the surface muon beam.

DOI: [10.1103/PhysRevAccelBeams.27.023403](https://doi.org/10.1103/PhysRevAccelBeams.27.023403)

### I. INTRODUCTION

The science case for muon sources is extensive, spanning research fields from fundamental particle physics, nuclear physics, and chemistry to condensed matter physics. Additionally, muon sources find broad applications in elemental analysis and energy research. Currently, four large-scale facilities worldwide provide muons for experiments and user instrumentation. These include the ISIS muon source at RAL (UK), the  $S\mu S$  at PSI (Swiss), the MUSE facility at J-PARC (Japan), and the CMMS muon source at TRIUMF (Canada), all actively contributing to condensed matter research [1]. Furthermore, PSI, J-PARC, and FNAL (USA) are engaged in broader muon programs in particle physics based on their muon source or dedicated muon beamlines. Several other accelerator facilities, such as CSNS (China), RAON (Korea), and SNS (USA), are either developing or considering a future muon source [2–4].

With the growing demand for more intense muon sources to enhance research capabilities and facilitate new discoveries [4,5], substantial efforts have been directed toward the

development or upgrade of accelerators, targets, beamlines, and detectors [6–15]. By optimizing the target and upgrading the beamline, the muon rate can be improved with a fixed proton beam current on the target. However, to achieve even higher intensity levels for muon sources, it is imperative to develop next-generation proton drivers.

In fact, the construction of a 500-MeV superconducting linac, designed for the accelerator-driven system (ADS) project, is currently underway in China [16]. The project, known as CiADS (Initiative Accelerator Driven Subcritical System), was initiated in 2021 to build a large-scale ADS experimental facility. The superconducting linac is specifically designed to accelerate a proton beam to 500 MeV with a current of 5 mA [17]. As part of the experimental facility, the subcritical reactor of CiADS is planned to operate for three months each year. Consequently, the proton beam will be available for other experiments and user terminals occupying a significant percentage of beam time.

The proposal for a high-intensity muon source driven by the CiADS linac has been under consideration for several years. From the perspective of beam power, such a muon source has the potential to be one of the state-of-the-art facilities. Exploring novel target ideas is essential to meet the challenges posed by unprecedented beam power. A large-aperture capture solenoid is also crucial for achieving a higher muon rate. This paper provides a brief introduction to the development of the superconducting linac in Sec. II. Sec. III introduces a new target concept based on a

\*Corresponding author: [hey@impcas.ac.cn](mailto:hey@impcas.ac.cn)

*Published by the American Physical Society under the terms of the Creative Commons Attribution 4.0 International license. Further distribution of this work must maintain attribution to the author(s) and the published article's title, journal citation, and DOI.*

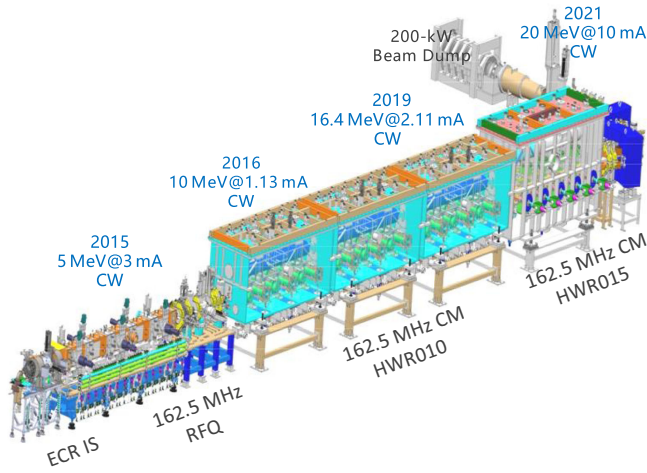


FIG. 1. Schematic view of the development and commissioning history of CAFe.

free-surface liquid lithium jet and investigates its performance in surface production. Section IV describes the investigation into capture efficiency, the effects of the capturing process, and the influence of capturing parameter sets. In Sec. V, a concise conclusion on the potential high-intensity muon source, consisting of next-generation technologies, is presented.

## II. DEVELOPMENT OF THE SUPERCONDUCTING LINAC

The development of the superconducting linac for ADS in China dates back to 2011. As illustrated in Fig. 1, the prototype front end linac (CAFe), mainly comprising an electron cyclotron resonance ion source, a radio frequency quadrupole (RFQ), a superconducting acceleration section, and a 200-kW beam dump, was developed incrementally. The commissioning of the hundred kW beam commenced in 2018 and achieved a milestone of a 20-MeV proton beam with an average current of 10 mA in early 2021 [18–21], successfully demonstrating the feasibility of a superconducting linac in continuous-wave (cw) mode.

Figure 2 presents the schematic diagram of the CiADS linac, which mainly consists of a normal conducting front end, a superconducting acceleration section, and several high-energy beam transport lines [22]. The front end comprises an ECR ion source, a low-energy beam

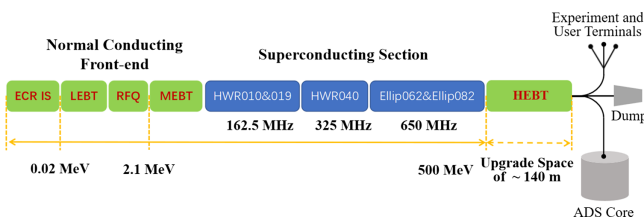


FIG. 2. Schematic diagram of the CiADS linac.

transport containing a fast chopper for beam pulse structuring and machine protection, an RFQ, and a medium-energy beam transport (MEBT). The proton beam out of the front end is a cw beam with a current of 5 mA and an energy of 2.1 MeV. After the MEBT, the superconducting section takes charge of the acceleration from 2.1 to 500 MeV. Three types of half wave superconducting resonators (HWR010, HWR019, and HWR040) and two types of elliptical cavities (Ellip062 and Ellip082) are housed in 32 cryomodules in the superconducting section [23,24].

The civil construction of the CiADS project is still underway, and the front end of the linac was integrated in December 2022 in a temporary laboratory. The beam commissioning has been carried out successfully with a proton beam out of the RFQ with an energy of 2.18 MeV and a current of 5.2 mA. According to the CiADS project schedule, the 500 MeV proton beam will be achieved by 2025, with a current of 50  $\mu$ A, and power ramping to 250 kW and 2.5 MW is expected to be achieved by 2027 and 2029, respectively. Alongside the muon source proposal, the upgrade of the superconducting linac to 600 MeV is also under consideration. In fact, the linac tunnel was designed to reserve a spare length of about 140 m to allow the upgrade of the linac to an energy of no less than 1.5 GeV, as shown in Fig. 2. In this article, the proton beam energy of 600 MeV will be used for the design studies.

## III. NEW TARGET SOLUTION

The production target of a high-intensity muon source is usually challenging due to high-heat density and a harsh irradiation environment [25]. The so-called surface muon possesses beneficial properties that can be utilized in various experiments. Arising from the two-body decay of positive pions stopped close to the surface of the production target, surface muons escape the target with a momentum ranging from 0 to 29.8 MeV/c. To facilitate the escape of muons, the production target of a muon source should be thin, and direct water cooling of the target through forced convection on the escaping surface should be avoided.

A rotating graphite target cooled by thermal radiation is currently the principal candidate for high-intensity muon sources driven by a proton beam with a beam power of several hundred kW or higher, such as  $S\mu$ S, MUSE, and the proposed ROAN  $\mu$ SR facility [26–28]. Graphite is chosen for its thermal, mechanical, and low-activation properties, as well as its high efficiency in muon production [29,30]. Based on the operational experience of the rotating target at PSI, the main disadvantage is the limited lifetime of the bearings, which have to operate without grease due to the harsh irradiation environment [26]. The beam power utilized by the target to produce muons depends mainly on beam energy, beam current, and target thickness in the beam direction. For a rotating target, it is challenging to be thick in the proton beam direction while keeping it thin for the surface muons to escape from a mechanical point of

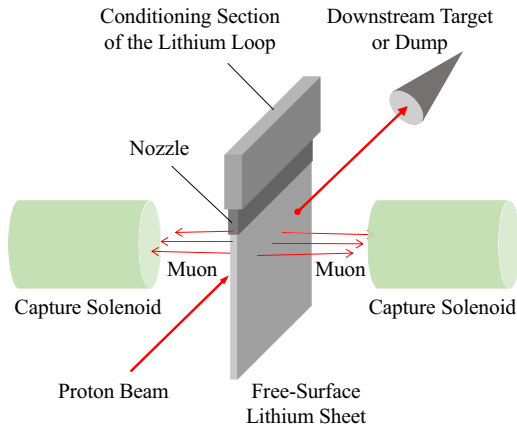


FIG. 3. Schematic diagram of the free-surface liquid lithium target.

view. The strength of the graphite rim poses the most important restrictions.

### A. Concept of free-surface lithium target

Here a novel concept based on a free-surface, sheet-shaped liquid lithium target (LiLiT) is proposed. As illustrated in Fig. 3, pressurized liquid lithium flows through the conditioning section of a lithium loop and finally forms a sheet-shaped jet from the narrow nozzle. The proton beam is collimated to hit the lithium jet at a small angle, and surface muons produced in lithium escape from either side of the sheet, entering the capture field of the solenoids.

Owing to its properties of low melting point, extremely low saturated vapor pressure, high heat capacity, and good compatibility with structural materials, liquid lithium has been widely used as a neutron production target [31,32], a radionuclide production target [33], and an ion beam charge stripper [34]. The main challenge is to maintain the stability of the free-surface liquid lithium sheet. Fortunately, numerous research and development efforts have been devoted to investigate the feasibility of producing free-surface liquid lithium films or sheets for applications in charge stripping [35], radionuclide production [33], and inertial fusion energy reactor chamber first-wall protection [36].

At Michigan State University (MSU), a 10–20- $\mu\text{m}$  thick liquid lithium jet flowing at  $>50$  m/s was created and confirmed stable when bombarded by various heavy ion beams [34]. To demonstrate the feasibility of a windowless lithium target for the rare isotope accelerator project, a liquid lithium jet with a cross section of 5 mm  $\times$  10 mm and a velocity varying up to 6 m/s was produced at Argonne National Laboratory (ANL), and thermal loads of up to 20 kW were applied to the jet by 1-MeV electron beams. It was demonstrated that the free-surface liquid lithium target flowing at a velocity of 1.8 m/s can operate stably without disruption or excess vaporization [37]. To investigate the stability of the high-speed liquid curtain shielding concept, which was proposed in the high-yield

lithium-injection fusion energy (HYLIFE-II) design to protect the first wall from the damaging radiation, a series of experiments using water as the simulant have been carried out. Free-surface fluctuations were quantified to be less than 5% over a wide range of distance from nozzle exit and flow dynamic parameters [38,39]. In fact, a stable jet with a height of several centimeters can meet the requirement of muon production. Thanks to the research efforts devoted by the teams of MSU, ANL, and HYLIFE-II, the feasibility of the free-surface liquid lithium target concept has, to a certain extent, been demonstrated, given that the Re-We parameter space (Reynolds number and Weber number) of the demanded liquid jet with a width of several millimeters and a velocity of several m/s is well covered by these experiments.

For the high-intensity muon source driven by CiADS linac, a liquid lithium target will be an excellent choice not only due to the properties mentioned above but also because of its low atomic number. Research performed at PSI indicates that the surface muon production efficiency is approximately proportional to  $Z^{-2/3}$  with  $Z$  being the atomic number [40]. Although it becomes more complicated when the geometric effects are considered, it can still be expected that the liquid jet target will perform well in terms of muon production efficiency.

A sheet-shaped jet, instead of a cylindrical one, as proposed for the neutrino factory or the muon collider [41,42], is chosen here not only for a higher ratio of side-leaking surface muons but also for a higher flow rate at the same velocity. With an rms beam size ( $\sigma_x/\sigma_y$ ) of 1 mm for the 600-MeV proton beam at 5 mA, the maximum heat density integrated with the jet direction is about 22 kW/cm<sup>2</sup>. With a jet velocity of 4 m/s, the maximum local temperature rise of the liquid lithium target is estimated to be less than 30 °C while the average temperature rise is around 10 °C. With a vaporization rate of about  $1 \times 10^{-7}$  g/(h cm<sup>2</sup>) at 230 °C [43] and a free area of 1000 cm<sup>2</sup>, the estimated evaporation rate will be 0.1 mg/h, which is same as that of the liquid lithium target (LiLiT) for neutron production and is expected to allow safe operation for long periods [32].

### B. Simulation framework and benchmarking

The simulation studies of surface muon production in this article were performed using the FLUKA program [44], based on the generally good agreement with the parametrization method [40] for pion production cross section. As shown in Fig. 4, below 150 MeV, the production cross section of  $\pi^+$  by FLUKA simulation is between 40% and 250% of that by parametrization for both graphite and lithium. The consistency is slightly better for the graphite target except for the divergence above 150 MeV at 60 deg. For the graphite target, data from proton beams of 585 MeV [45] and 590 MeV [46] are given for comparison. The accuracy of the parametrization is of the order of 10%.

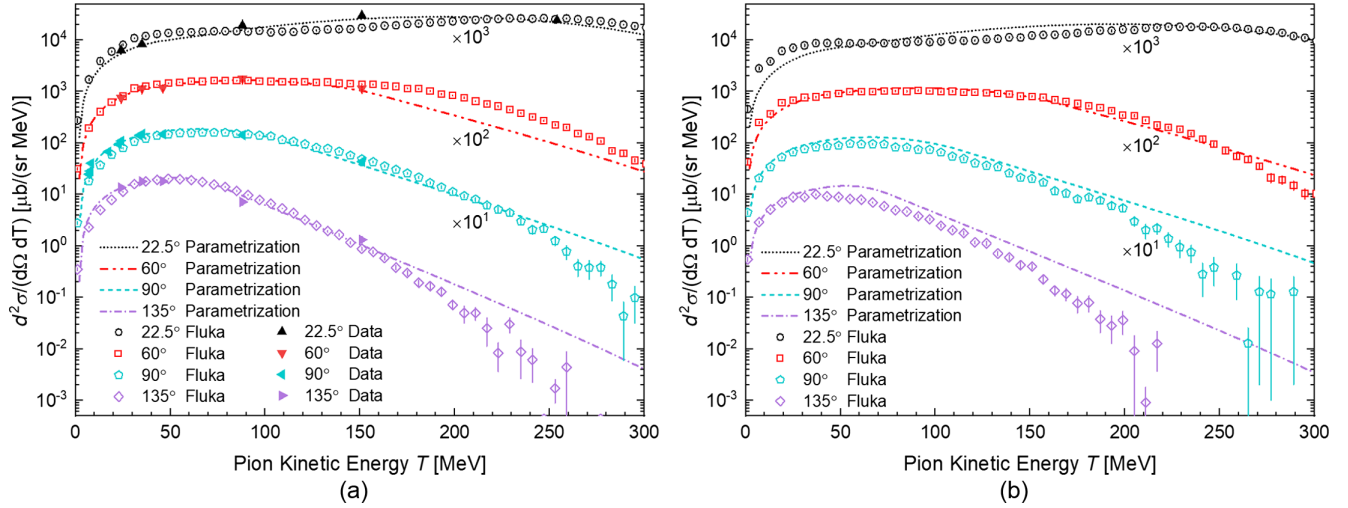


FIG. 4. (a) Simulated double-differential cross sections of  $\pi^+$  production from graphite target at a proton energy of 585 MeV using FLUKA in comparison to the results of the parametrization method from [40] and data from [45,46]. (b) Same as (a) except that the target is lithium, the proton beam energy is 600 MeV, and no data are given.

Although the FLUKA simulation is slightly less good, it is still in the same order of magnitude.

The so-called generalized intranuclear cascade (GINC) model is used in the FLUKA program for the hadron-nucleus interactions at momenta below 3–5 GeV/c. As an intranuclear cascade (INC) model, the GINC model relies on the hadron-nucleon cross sections represented by parameterized fits based on available experimental data [47] to describe resonance production and decay processes. The hadron-nucleon cross sections usually are modified to involve nuclear-medium effect. Unlike the INC models, the parametrization methods are provided to predict the double-differential  $\pi^+$  production cross sections of hadron-nucleus interactions directly. The one used in this article is given by Berg *et al.* [40], combining the first parametrization [48], which is only valid for low pion kinetic energies below 40 MeV and reactions on carbon at proton energies of 580 MeV, and the second parametrization [49], which is valid for all elements and all pion energies at proton energies below 800 MeV. These parametrizations were developed based on the detailed measurements of pion production cross sections performed in the early years of meson factories [45,46,50,51]. In these experiments, various target nuclei, such as H, D, Be, C, O, Al, Ti, Ni, Cu, Mo, Ag, Ta, Pb, and Th were investigated while the Li target was not involved.

Compared to the parametrization model, for  $\pi^+$  below 100 MeV, which is of the greatest importance in surface muon production, the FLUKA simulation tends to overestimate the  $\pi^+$  production cross sections at the angles of 22.5° and 60°, while giving a lower estimation at 90° and 135°. This tendency applies to both the graphite target and the lithium target. To figure out the difference in total surface muon yields by FLUKA and parametrization, the high-intensity muon beams (HIMB) graphite target [52] is chosen

for comparison. The surface muon rate of the 585-MeV proton is estimated to be  $5.7 \times 10^{-6} \mu^+/\text{p}$  by FLUKA, which is about 16% less than that given by the GEANT4 simulation based on the pion production cross section from parametrization [52]. For a lithium target, detailed measurements of pion production cross sections in the future are essential for a more reliable prediction of the surface muon yield.

### C. Geometry optimization

It has been demonstrated that a significant gain of 50% or even more in the surface muon rate can be achieved by implementing a small slant angle on the slab target [40,52]. The essential idea is to increase the percentage of the stopping pions while allowing the surface muons to escape more easily. Figure 5 illustrates the beam-target geometry for the slanted slab target. The proton beam penetrates straight through the target while the secondary pions can be stopped along the whole length of  $L$ . If not slanted, the width of the slab should be at least several times the rms size ( $\sigma_x/\sigma_y$ ) of the beam spot. This value can be smaller in the slanted geometry to facilitate the escape of surface muons. For the key dimensions denoted and marked in red, the following equations are listed:

$$W = L \tan \theta - 2D / \cos \theta, \quad (1)$$

$$L = T \cos \theta + 2D / \sin \theta, \quad (2)$$

$$T = W / \sin \theta. \quad (3)$$

With a jet length ( $L$ ) of 25 cm and a gap ( $D$ ) of 5 mm to ensure space for the proton beam on the liquid lithium jet target, the width ( $W$ ) and the corresponding effective

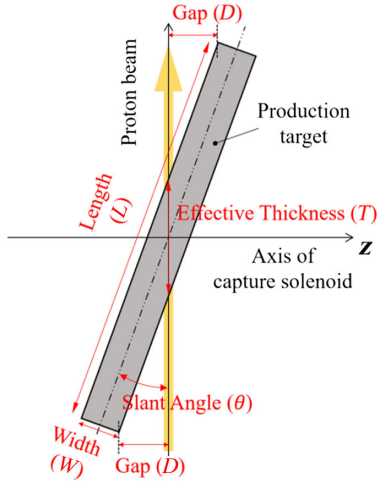


FIG. 5. Schematic diagram of the beam-target geometry with key dimensions denoted and marked in red.

thickness ( $T$ ) in proton beam direction as functions of slant angle ( $\theta$ ) are shown in Fig. 6(a).

With a fixed length ( $L$ ) and a fixed gap ( $D$ ), the width and thus the effective thickness can be increased by rotation for a larger slant angle. It is easy to understand that the increase in the effective thickness tends to be less sharp than the increase in width for a larger slant angle. As a result, the gain in muon rate from the increase in slant angle will be less significant. It is illustrated in Fig. 6(b) that the larger the gap ( $D$ ) is, the smaller the effective thickness ( $T$ ) will be for a specific width. On the contrary,  $T$  has a positive correlation with  $L$ .

As shown in Fig. 6(b), the jet with  $L = 25$  cm and  $D = 5$  mm and that with  $L = 35$  cm and  $D = 7.5$  cm are similar in effective thickness at a width below 1 cm. Here the length of 25 cm and the gap of 5 mm are chosen to investigate the surface muon rate. With  $\sigma_x = \sigma_y = 1$  mm

and a zero divergence, the 600-MeV proton beam is used to impact the lithium slab target with different slant angles. The surface muons from the target are recorded by a virtual detector (det1) placed centrally at a distance of 3 cm from the target, parallel to the proton beam. The virtual detector is 50 cm in diameter to cover most of the side-leaking surface muons. The muon rate is normalized to the effective thickness to obtain  $NR_{\text{det1}}$ .

As shown in Fig. 7, the surface muon rate ( $R_{\text{det1}}$ ) slowly increases to a maximum of  $1.7 \times 10^{-5} \mu^+/\text{p}$  at the angle of  $6^\circ$ , maintaining a saturated value as the slant angle increases further. In addition to thickness, the width that determines both the pion stopping rate and muon escaping efficiency is also crucial for the surface muon rate. A small target width will result in a small pion stop rate while a large one is adverse for muon escaping. From the perspective of the rate per unit target thickness, the optimal slant angle is  $3^\circ$ , where the effective thickness is 5.9 cm and the normalized surface muon rate is  $1.67 \times 10^{-6} \mu^+/\text{(p cm)}$ . The decrease after the slant angle of  $3^\circ$  indicates that the detrimental effect of a large target width is dominating the surface muon production efficiency.

#### D. Comparison with graphite target

The effective thickness of the HIMB graphite target is 2 cm. With a slant angle of  $10^\circ$  and a width of 3.5 mm, the target geometry is considered optimal from the point of view of muon rate and mechanical feasibility after exploring various design versions. For the CiADS muon source, the optimization logic should be the same if a rotating graphite target and a slant geometry are adopted. In fact, gaining muon rate from an increase in target thickness will be challenging, not only due to mechanical feasibility but also because the proton beam current of CiADS is more than two times higher. With a similar beam energy of

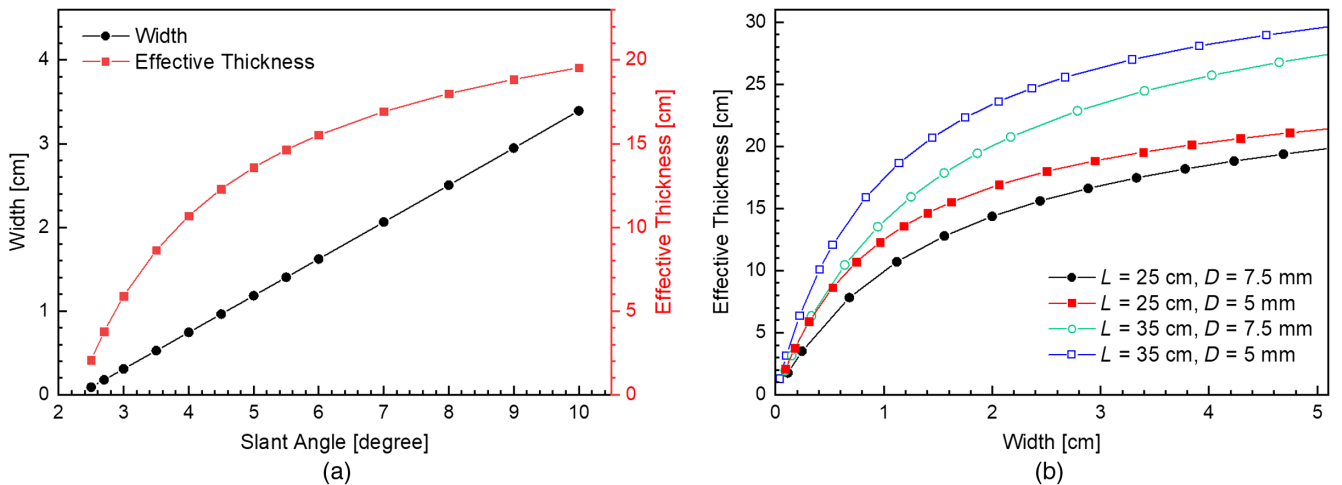


FIG. 6. (a) Width ( $W$ ) and effective thickness ( $T$ ) as functions of slant angle for the jet with a length ( $L$ ) of 25 cm, and a gap ( $D$ ) of 5 mm. (b) The effective thickness as functions of the width for four sets of  $L$  and  $D$ .

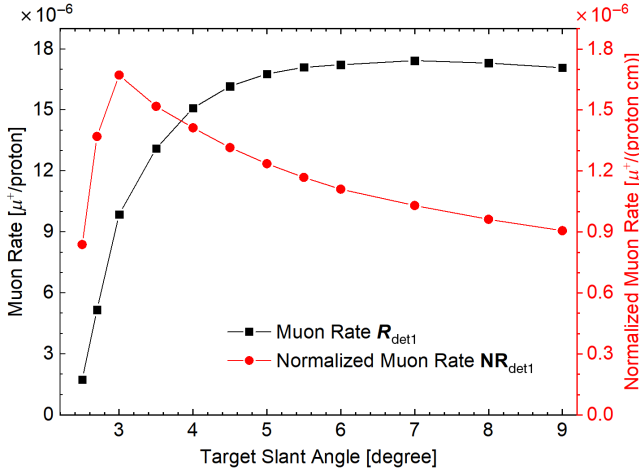


FIG. 7. Surface muon rate from the lithium target with a jet length ( $L$ ) of 25 cm at different slant angles, maintaining a fixed gap ( $D$ ) of 5 mm while varying width and effective thickness. The normalized surface muon rate ( $NR_{\text{det1}}$ ) is given in the right scale.

600 MeV, the heat power deposited in the target will be more than twice as high.

Unlike the rotating graphite target, the lithium jet target is much more flexible for optimizing the slant angle and the length because it will not be restricted by the wheel structure, rim strength, and space limitations. For the comparison of the muon rate from the lithium target to that from the 2-cm graphite target, the effective thickness of the lithium target was chosen to guarantee a similar beam energy loss. Here, the density of the graphite is set to  $1.84 \text{ g/cm}^3$  while that of lithium is set to  $0.515 \text{ g/cm}^3$ . Through FLUKA simulation, we found that both the energy distribution peaks of the proton beams penetrating the 7.8-cm lithium target and the 2-cm graphite target are located at 591.9 MeV. It is shown in Fig. 6(a) that the thickness at the slant angle of  $3.5^\circ$  is 8.6 cm for the parameter set of  $L = 25 \text{ cm}$  &  $D = 5 \text{ mm}$ . If we increase the gap ( $D$ ) to 5.25 mm, the width decreases slightly to 4.8 mm and the effective thickness decreases to 7.8 cm. As shown in Fig. 8, the energy distributions of the proton beams are almost the same after penetrating the two targets. Therefore, it is reasonable to assume that the downstream beam losses caused by energy loss and multiple scattering in the target will be close.

Figure 9 presents the momentum spectra of the side-leaking  $\mu^+$ ,  $\pi^+$ , and  $e^+$  recorded by the detector beside the target for both lithium and graphite targets. It can be seen that the lithium target produces more low-energy  $\pi^+$  and, consequently, more surface muons than the graphite target, while the rate of positrons is much smaller. As shown in Fig. 9, both the high-energy positrons from gamma and  $\pi^0$  and the medium-energy step with an endpoint energy of 52.8 MeV from the free Michel decay of the  $\mu^+$  at rest is about 50% less for the lithium target. Additionally, the lithium target can avoid vast low-energy

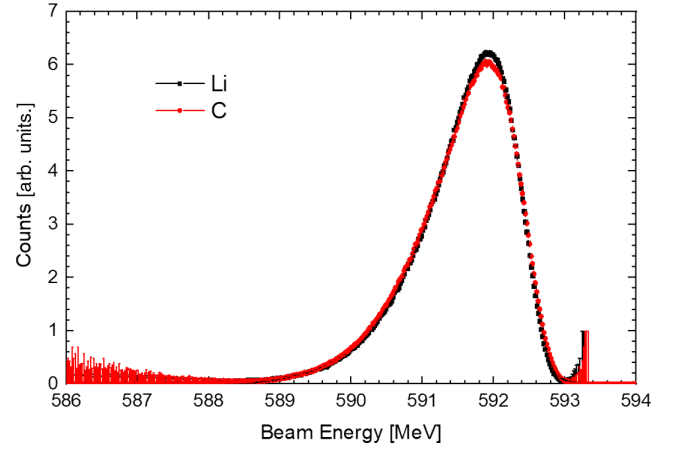


FIG. 8. Energy distributions of the proton beams penetrating the 7.8-cm lithium target and the 2-cm graphite target.

positrons from the  $\beta^+$  decay of radioactive isotopes. According to the fluka simulation, short-lived isotopes, such as  $^8\text{B}$ ,  $^9\text{C}$ , and  $^{12}\text{N}$  and medium-lived ones like  $^{10}\text{C}$ ,  $^{11}\text{C}$ , and  $^{13}\text{N}$  are produced in the graphite target, contributing the majority of the positrons below 15 MeV/c. Around the momentum peak of the surface muons at 28.7 MeV/c, the ratio of positrons to muons is 0.65 and 2.8 for lithium and graphite, respectively. A lower positron-muon ratio is expected to make the background separation less challenging. This is advantageous for the typical applications of the muon spin spectroscopy method ( $\mu\text{SR}$ ) in solid-state physics, chemistry, and material science, as it is based on the detection of the positrons generated by the decay of muons at rest in a sample. Additionally, experiments aiming to search for charged lepton flavor violation channels, such as  $\mu^+ \rightarrow e^+e^+e^-$  and  $\mu^+ \rightarrow e^+\gamma$ , will also benefit from the lower positron-muon ratio.

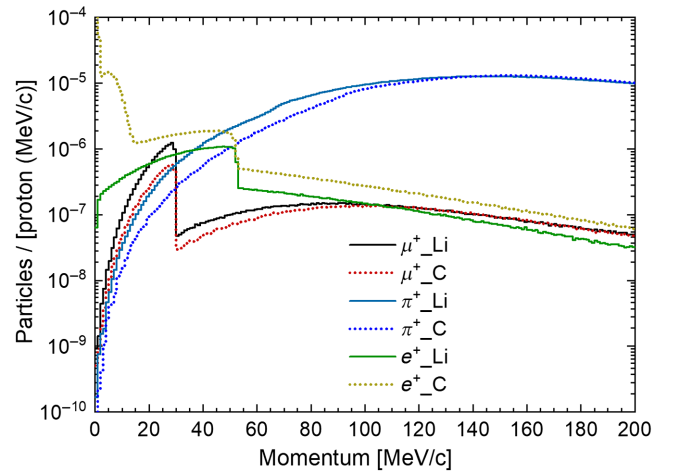


FIG. 9. Momentum spectra of  $\mu^+$  and  $\pi^+$  and  $e^+$  recorded by the virtual detector det1 beside the target.

TABLE I. Main characteristics of the initial muon beams from the two targets.

	2-cm graphite	7.8-cm lithium	Unit
$I_{\text{det}1}$	0.57	1.22	$10^{-5} \mu^+/\text{p}$
$\varepsilon_x(1\sigma)/\varepsilon_y(1\sigma)$	506/548	767/571	$\pi \text{ cm mrad}$
Polz	66.8	66.9	%

Here we focus on the muons below 30 MeV/c, most of which are surface muons. In the following sections, the muons below 30 MeV/c will be referred to as surface muons or simply as muons for simplicity. Table I gives a summary of the rate ( $I_{\text{det}1}$ ), rms emittance ( $\varepsilon_x$  and  $\varepsilon_y$ ), and the mean value of the spin polarization with respect to the longitudinal axis (Polz) of the target muon beam. As shown in Table I, the surface muon rate from the 7.8-cm lithium target is  $1.22 \times 10^{-5} \mu^+/\text{p}$ , which is about 2.1 times that from the 2-cm graphite target. The axial polarization is almost the same for the two targets. The horizontal emittance of the muons from the lithium target is about 50% larger due to a larger thickness in the proton beam direction. This is well illustrated in Fig. 10, where the lithium target provides the surface muon beam with a larger standard deviation of the position distribution in the horizontal direction. All other parameters are very close.

The asymmetry of the horizontal position distribution is even less significant for the lithium target owing to the smaller slant angle and target density.

Because the density of lithium is much lower, the effective thickness of the lithium target would need to be about four times larger than that of the graphite target to maintain the same proton beam utilization rate. A longer target tends to result in a larger emittance, which could be detrimental to the capture and transmission of the muon beam. Therefore, it is necessary to investigate the influence of the target thickness on the main characteristics of the muon beam after the capture solenoid, and this will be described in the next section.

## VI. CAPTURE SCHEME

The conventional capture approach, using a quadrupole doublet or triplet, typically achieves a capture efficiency at the level of 5%. It has been demonstrated that a five-fold increase in capture efficiency can be achieved by employing a large-aperture solenoid [52]. In this context, a radiation-hard normal conducting solenoid with a channel aperture of 50 cm and a coil length of 40 cm is used as the baseline option. While the acceptance of the capture channel is determined solely by the parameter set of the solenoid and the capture layout, the effects of the capturing

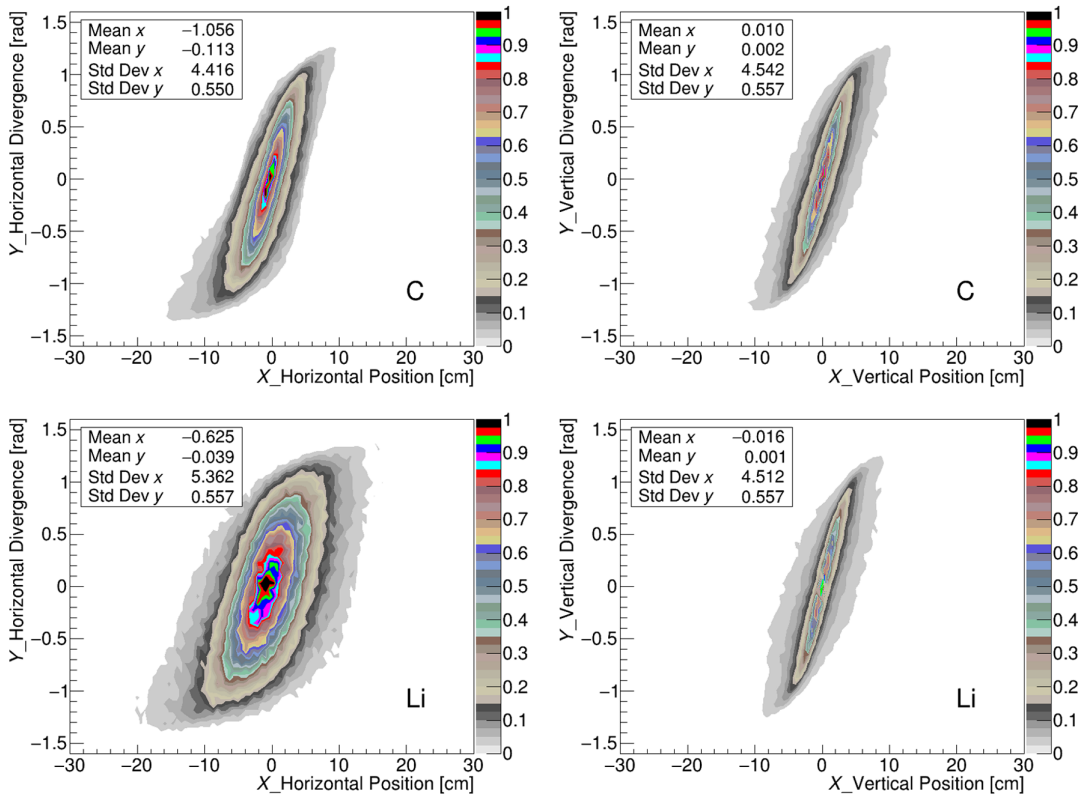


FIG. 10. Phase space distributions of the surface muon beam from the 2-cm graphite target (top) and the 7.8-cm lithium target (bottom), which are recorded by the detector beside the target.

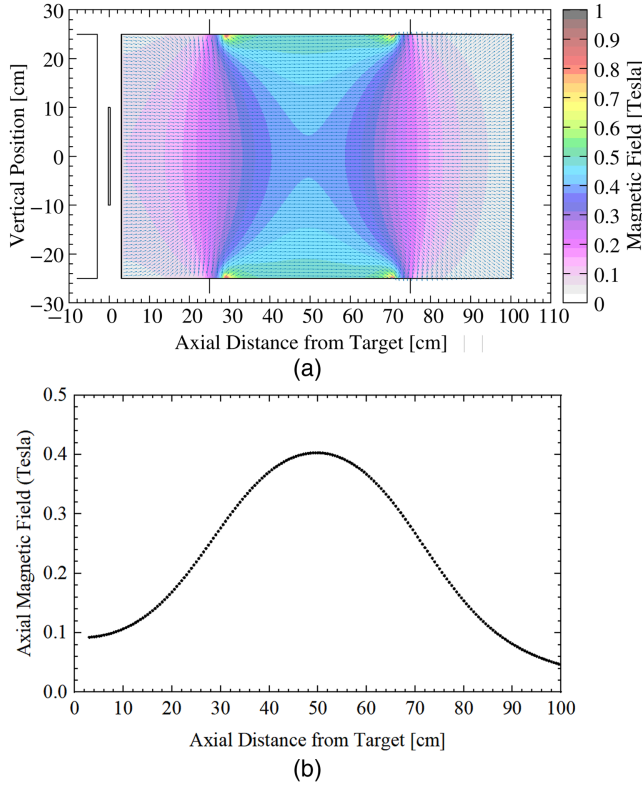


FIG. 11. (a) Capture magnetic field map in the horizontal cross section at proton beam height. (b) Distribution of axial magnetic field  $B_z$  along the central axis of the solenoid.

process will also depend on the momentum distribution as well as the emittance of the muon beam from the target.

### A. Capture efficiency for different target lengths

Two solenoids are symmetrically positioned on both sides of the lithium sheet. As shown in Fig. 11, this paper focuses only on the capture process on the right-hand side of the target in the proton beam direction. The magnetic field produced by both capture solenoids is applied. With the distance between the target and the first coil of the capture solenoids being 30 cm, investigations into surface muon rates before and after the solenoid are performed for different target thicknesses in the proton beam direction. The capture magnetic field in the horizontal cross section at proton beam height is shown in Fig. 11(a). The distribution of the axial magnetic field along the central axis of the capture solenoids is shown in Fig. 11(b). It can be seen that the maximum field is approximately 0.4 Tesla, which is achievable with normal conducting solenoids in the current design.

In the simulation, the lithium slab target with a fixed width of 10 mm varies in length, and the slant angle is set to zero for simplicity. Another virtual detector det2 also with a diameter of 50 cm, is placed at 100 cm from the target, on the downstream side of the solenoid to detect the captured surface muons. A Gaussian proton beam spot with  $\sigma_x = \sigma_y = 1$  mm is used. Surface muons recorded by the two

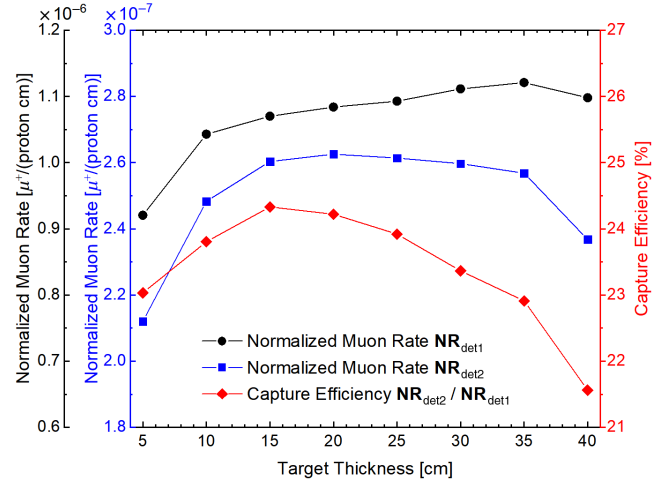


FIG. 12. Normalized surface muon rates and the capture efficiencies as functions of lithium target thickness. The normalized surface muon rates  $NR_{\text{det1}}$  and  $NR_{\text{det2}}$  are given in the first left scale and the second left one, respectively. The capture efficiency  $NR_{\text{det2}}/NR_{\text{det1}}$  is given in the right scale.

detectors are normalized to the target thickness to obtain  $NR_{\text{det1}}$  and  $NR_{\text{det2}}$ . Here the thickness is actually the target length since no rotation is applied.

As shown in Fig. 12, the normalized muon rate from the target,  $NR_{\text{det1}}$ , increases to a maximum of  $1.1 \times 10^{-6} \mu^+/(p \text{ cm})$ , representing a percentage increase of more than 20% when the target thickness varies from 5 to 35 cm. This is mainly attributed to the increase in the stopping rate of forward and backward pions. For comparison, the turning point of  $NR_{\text{det2}}$  appears at a target thickness of 20 cm, where the normalized muon rate is  $2.63 \times 10^{-7} \mu^+/(p \text{ cm})$ , earlier than that of  $NR_{\text{det1}}$ . The capture efficiency defined by  $NR_{\text{det2}}/NR_{\text{det1}}$  increases to a maximum of 24.3% at a target thickness of 15 cm. This is due to the gain in the percentage of side-facing muons. For larger thicknesses, the capture efficiency decreases due to the increase of emittance. More generally, both the normalized muon rates and the capture efficiency vary by less than 7% in a wide thickness range from 10 to 35 cm. Therefore, it is reasonable to believe that the low density of lithium will not result in a significant disadvantage in the capture efficiency when a large-aperture solenoid is equipped.

### B. Capturing effects

After the capture solenoid, the muon beams from the two targets are recorded for further comparison. It is interesting to note that the distribution in phase space is very similar after the solenoid, as shown in Fig. 13. Table II gives a summary of the rate, emittance, and axial polarization of the captured muon beam. The similarity of the emittance once again illustrates that the large-aperture solenoid nearly eliminates the difference of the distribution in phase space.

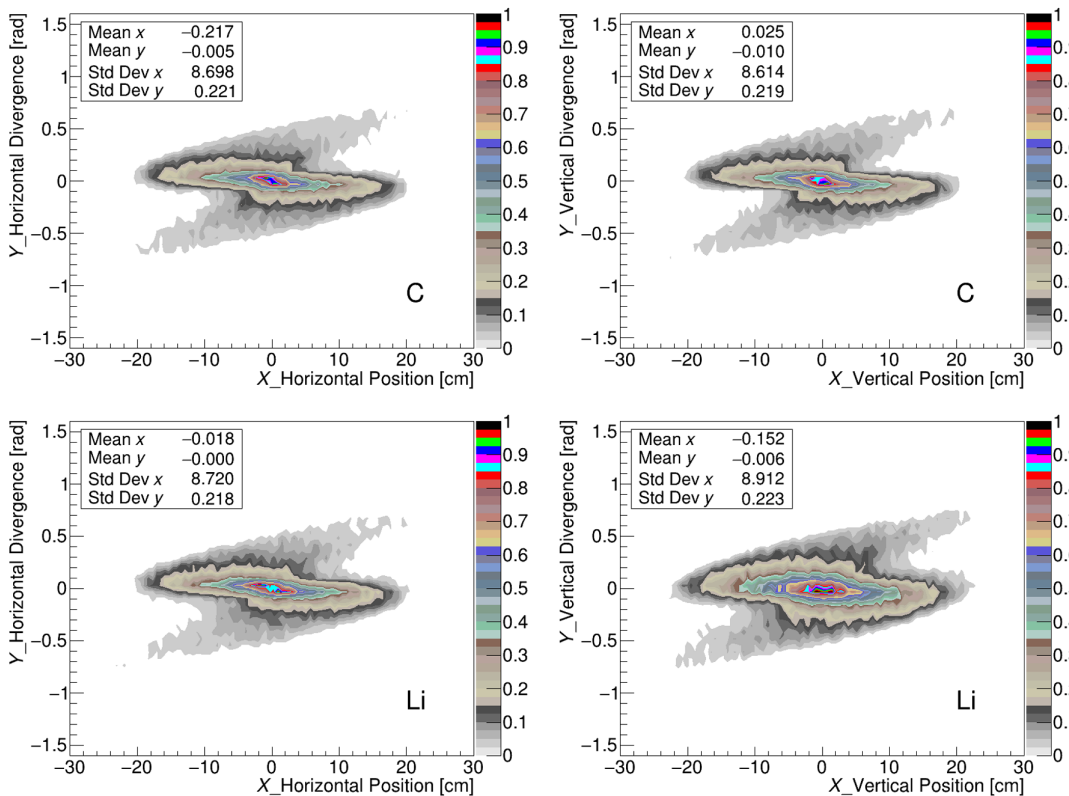


FIG. 13. Same as Fig. 10 except that the detector is downstream of the solenoid.

The ratio of the muon rates from the two targets is almost the same as that upstream of the solenoid, which means that the capture efficiencies are very close, as can be expected.

For both targets, the axial polarization increases from 67% to around 93% after the capture solenoid. This is likely due to the selection of the momentum direction by solenoid. As shown in Fig. 14, the momentum distributions vary by a small magnitude while the distributions of the axial momentum and polarization are significantly reshaped. For surface muons which are 100% polarized, the distribution of the spin polarization with respect to the longitudinal axis and that of the axial component of direction vector is exactly symmetric. It is illustrated in Figs. 14(c) and 14(d) that the decay muons slightly break the symmetry of the distributions.

Considering the negligible impact of target thickness on the capture efficiency of surface muons until it becomes comparable with the solenoid aperture, and the remarkable

similarity in transverse phase space distribution and momentum distribution after the capture solenoid, we can now conclude that the front end configuration, consisting of an liquid lithium target and a large-aperture capture solenoid, can achieve a higher muon rate without compromising other aspects of performance.

### C. Capturing parameter set

The solenoid aperture, field strength, and the distance between the coil and the target are the main determining factors in the capturing process. Owing to its compactness, it is feasible for the lithium target to be closer to the coil. As summarized in Table III, the rate after the solenoid increases by 50%, and the emittances in both the horizontal and vertical planes decrease by around 15% when the distance is shortened from 30 to 10 cm. The polarization also experiences a slight increase. Theoretically, further gain in capture efficiency and other aspects of performance can be achieved if the lithium target is enclosed by the solenoid. However, this poses a significant challenge, whether the lithium jet is sheet-shaped or cylindrical. Although the technical feasibility of the free-surface mercury jet target, which was designed to be enclosed by the capture solenoid [53], has been demonstrated by the MERIT experiment at the CERN PS [54,55], the idea of a slab target paired with two large-aperture solenoids is more realistic for a surface muon source, where both the jet and

TABLE II. Main characteristics of captured surface muon beams for the two targets.

	2-cm graphite	7.8-cm lithium	Unit
$I_{\text{det}2}$	1.38	2.97	$10^{-6} \mu^+/p$
$\varepsilon_x(1\sigma)/\varepsilon_y(1\sigma)$	605/597	603/629	$\pi \text{ cm mrad}$
Polz	92.8	93.2	%

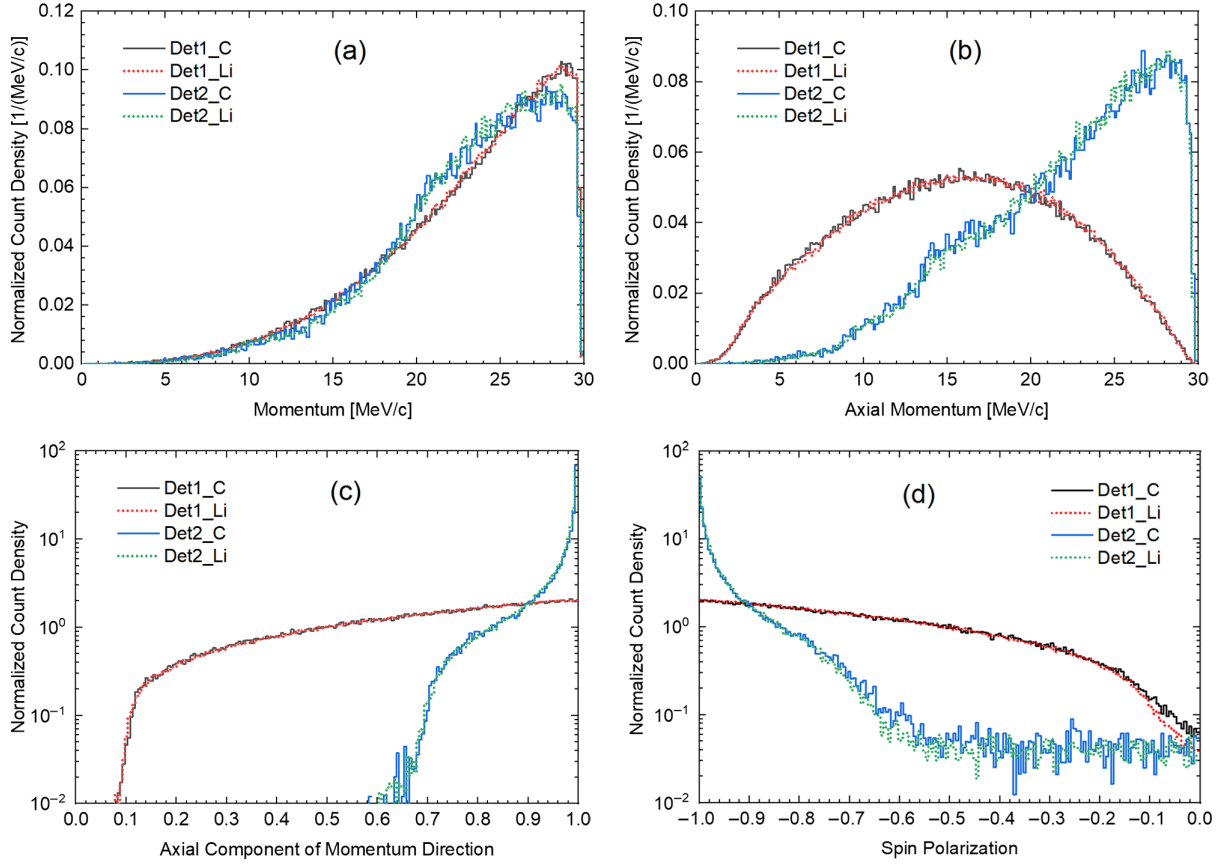


FIG. 14. Momentum and polarization distributions of the muon beams before and after the capture solenoid. The solid lines for the 2-cm graphite target and the short-dot lines for the 7.8-cm lithium target. (a) Momentum distribution. (b) The distribution of the axial component of momentum. (c) The distribution of the axial component of direction vector. (d) The distribution of the spin polarization with respect to the longitudinal axis.

proton beam are outside the solenoid. In fact, the two solenoids on both sides can be considered as a single solenoid split by the target, allowing the incident proton beam to penetrate the slab target transversely, and the surface of the target to be oriented toward the axial-focusing channel of muons.

TABLE III. Main characteristics of the surface muon beams from the 7.8-cm lithium target with different parameter sets for capture solenoid.

Aperture 50 cm	Distance between target and coil			Unit
	30 cm	20 cm	10 cm	
$R_{\text{det2}}$	2.97	3.74	4.45	$10^{-6} \mu^+/\text{p}$
$\varepsilon_x(1\sigma)/\varepsilon_y(1\sigma)$	603/629	561/587	526/544	$\pi \text{ cm mrad}$
Polz	93.2	94.6	95.5	%

Aperture 40 cm	Distance between target and coil			Unit
	30 cm	20 cm	10 cm	
$R_{\text{det2}}$	2.21	2.89	3.78	$10^{-6} \mu^+/\text{p}$
$\varepsilon_x(1\sigma)/\varepsilon_y(1\sigma)$	407/431	379/405	368/384	$\pi \text{ cm mrad}$
Polz	93.2	94.7	95.9	%

When the solenoid sits close enough, it is possible to use a capture solenoid with a smaller aperture to reduce the emittance while maintaining the muon rate above a reasonably high level. The bottom half of Table III lists the main characteristics of the muon beam after the 40-cm-aperture solenoid. The limiting magnetic field is nearly inversely proportional to the aperture of solenoid. Therefore, the reduction in aperture, to a certain extent, can be balanced by the advantage of a higher magnetic field. For simplicity, the magnetic field is scaled with a factor of 1.25 for the 40-cm solenoid. As shown in this table, the emittance decreases by more than 40% for all three situations when the solenoid aperture decreases from 50 to 40 cm. It is interesting to note that the loss in muon rate is obviously smaller for the situation of distance = 10 cm, which is only 15%, whereas that for the situation of distance = 30 cm is 34%. It seems even more advantageous for the 40-cm solenoid to sit closer to the target: the muon rate increases by 70% when the distance is shortened to 10 from 30 cm.

It can be expected that a smaller emittance will result in a gain in downstream transmission efficiency and a factor that still needs exploration in the design studies of muon

beamlines. A concern related to the distance is the potential influence on the lithium jet from the fringing field produced by the capture solenoids. The advantage of the lithium target is a larger space for the mirror plates in front of the capture solenoid to reduce the magnetic field seen by the target. In the worst-case scenario, where a stable liquid jet is unachievable due to the existence of a partially canceled fringing field, the polarity of the two capture solenoids can be set to be inverse, and thus their magnetic fields at the target shall cancel if symmetry is well maintained.

## V. CONCLUSION

To meet the requirement of the next-generation muon source driven by cw superconducting linac, a new solution for the muon production target is essential. In comparison to the rotating graphite target, the lithium jet target proposed in this paper offers advantages in surface muon production efficiency, heat-removal ability, and target geometry compactness. Simulation studies demonstrate that the front end, consisting of a lithium jet and a capture solenoid, can provide more surface muons for the downstream muon beamline. When the 600-MeV proton beam is equipped with the front end, a muon rate of no less than  $4 \times 10^{-6} \mu^+/\text{p}$  can be obtained at the exit of the capture solenoid. A transmission efficiency of 40% may be achieved by the downstream beamline based on solenoid and larger-aperture bending magnets. Therefore, the surface muon beam with an unprecedented rate of  $5 \times 10^{10} \mu^+/\text{s}$  can be delivered to the experimental area or further manipulation section, at the proton beam current of 5 mA. We believe this will enable entirely new experiments with considerable discovery potential and unique sensitivities in particle physics, condensed matter physics, and materials science.

## ACKNOWLEDGMENTS

Fruitful discussions with Professor Jingyu Tang are gratefully acknowledged. This work is supported by the National Development and Reform Commission of China (Large Research Infrastructures of 12th Five-Year Plan: China initiative Accelerator Driven System, Grant No. 2017-000052-75-01-000590).

- 
- [1] A. D. Hillier, S. J. Blundell, I. McKenzie *et al.*, Muon spin spectroscopy, *Nat. Rev. Methods Primers* **2**, 4 (2022).
  - [2] Y. Bao, J. Chen, C. Chen *et al.*, Progress report on Muon Source Project at CSNS, *J. Phys. Conf. Ser.* **2462**, 012034 (2023).
  - [3] Y. J. Kim, Current status of experimental facilities at RAON, *Nucl. Instrum. Methods Phys. Res., Sect. B* **463**, 408 (2020).
  - [4] D. Louca, G. J. MacDougall, and T. J. Williams, Report from: US Muon Workshop 2021: A road map for a Future

- Muon Facility, February 1-2, 2021, *Neutron News* **33**, 8 (2022).
- [5] M. Aiba, A. Amato, A. Antognini *et al.*, Science case for the new high-intensity muon beams HIMB at PSI, [arXiv:2111.05788](https://arxiv.org/abs/2111.05788).
- [6] W. Higemoto, R. Kadono, N. Kawamura *et al.*, Materials and life science experimental facility at the Japan Proton Accelerator Research Complex IV: The muon facility, *Quantum Beam Sci.* **1**, 11 (2017).
- [7] J. Grillenberger, C. Baumgarten, and M. Seidel, The high intensity proton accelerator facility, *SciPost Phys. Proc.* **5**, 002 (2021).
- [8] A. Bungau, R. Cywinski, C. Bungau, P. King, and J. Lord, Simulations of surface muon production in graphite targets, *Phys. Rev. ST Accel. Beams* **16**, 014701 (2013).
- [9] S. Makimura, S. Matoba, N. Kawamura *et al.*, Perspective of muon production target at J-PARC MLF MUSE, *J. Phys. Soc. Jpn. Conf. Proc.* **21**, 011058 (2018).
- [10] L. P. Zhou, X. J. Ni, Z. Salman, A. Suter, J.-Y. Tang, V. Vrankovic, and T. Prokscha, Simulation studies for upgrading a high-intensity surface muon beamline at Paul Scherrer Institute, *Phys. Rev. Accel. Beams* **25**, 051601 (2022).
- [11] N. Kawamura, M. Aoki, J. Doornbos *et al.*, New concept for a large-acceptance general-purpose muon beamline, *Prog. Theor. Exp. Phys.* **2018**, 113G01 (2018).
- [12] G. D. Maso, F. Barchetti, M. Francesconi *et al.*, Beam monitoring detectors for High Intensity Muon Beams, *Nucl. Instrum. Methods Phys. Res., Sect. A* **1047**, 167739 (2023).
- [13] G. D. Maso, A. Gabard, M. H. Tahar *et al.*, Future facilities at PSI, the High-Intensity Muon Beams (HIMB) project, *Eur. Phys. J. Web Conf.* **282**, 01012 (2023).
- [14] D. Kiselev, P. Baumann, P.-A. Duperrex *et al.*, The PSI meson target facility and its upgrade IMPACT-HIMB, in *Proceedings of the EPJ Web of Conferences on the 30th Conference of the International Nuclear Target Development Society (INTDS2022)* (EDP Sciences, Les Ulis, France, 2023), p. 07002.
- [15] E. Valetov, Beamline design and optimization for high intensity muon beams at PSI, *J. Phys. Conf. Ser.* **2420**, 012053 (2023).
- [16] Y. He, H. Jia, X. Zhang *et al.*, Accelerator driven system—A solution to multiple problems of society, in *Proceedings of 14th International Particle Accelerator Conference, Venice, Italy, 2023* (JACoW, Geneva, Switzerland, 2023), p. 5205.
- [17] Z. J. Wang, F. F. Wang, G. R. Huang *et al.*, The status of CiADS superconducting linac, in *Proceedings of the 10th International Particle Accelerator Conference. Melbourne, Australia, 2019* (JACoW, Geneva, Switzerland, 2019), p. 994.
- [18] Y. He, Progress and operation experience at CAFe, in *Proceedings of the 20th International Conference on RF Superconductivity (SRF'2021)*, East Lansing, MI (CERN, Geneva, Switzerland, 2021).
- [19] Z. J. Wang, The beam commissioning of 10 mA, 100 kW CW proton beam at CAFe, in *Proceedings of the 14th International Particle Accelerator Conference, Venice, Italy* (JACoW, Geneva, Switzerland, 2023).

- [20] S. Liu, Z. Wang, W. Chen *et al.*, Commissioning of China ADS demo Linac and baseline design of CiADS project, *J. Phys. Conf. Ser.* **1401**, 012009 (2020).
- [21] H. Jia, H. Niu, H.-J. Cai *et al.*, Design and development of the 200-kW beam dump, *Nucl. Sci. Eng.* **198**, 64 (2023).
- [22] Z. Wang, S. Liu, W. Chen *et al.*, Beam physics design of a superconducting linac, *Phys. Rev. Accel. Beams* **27**, 010101 (2024).
- [23] S. Liu, Z. Wang, Y. Tao *et al.*, Physics design of the superconducting section of the CiADS linac, *Int. J. Mod. Phys. A* **34**, 1950178 (2019).
- [24] Y. L. Huang, L. B. Liu, T. C. Jiang *et al.*, 650 MHz elliptical superconducting RF cavities for CiADS Project, *Nucl. Instrum. Methods Phys. Res., Sect. A* **988**, 164906 (2021).
- [25] D. Kiselev, P. Baumann, and P. Duperrex *et al.*, Progress and challenges of the PSI meson targets and relevant systems, *J. Phys. Soc. Jpn. Conf. Proc.* **33**, 011102 (2021).
- [26] D. Kiselev, P. A. Duperrex, S. Jollet *et al.*, The meson production targets in the high energy beamline of HIPA at PSI, *SciPost Phys. Proc.* **5**, 003 (2021).
- [27] S. Makimura, N. Kawamura, S. Onizawa *et al.*, Development of muon rotating target at J-PARC/MUSE, *J. Radioanal. Nucl. Chem.* **305**, 811 (2015).
- [28] J. Y. Jeong, J. C. Kim, Y. Kim *et al.*, Design of muon production target system for the RAON  $\mu$ SR facility in Korea, *Nucl. Eng. Technol.* **53**, 2909 (2021).
- [29] E. W. Blackmore, A. Dowling, R. Ruegg *et al.*, Operating experience with meson production targets at TRIUMF, in *Proceedings of the 21st Particle Accelerator Conference, Knoxville, TN, 2005* (IEEE, Piscataway, NJ, 2005), p. 1919.
- [30] A. Bungau, R. Cywinski, C. Bungau *et al.*, Target optimization studies for surface muon production, *Phys. Rev. ST Accel. Beams* **17**, 034701 (2014).
- [31] H. Kondo, T. Kanemura, T. Furukawa *et al.*, Validation of IFMIF liquid Li target for IFMIF/EVEDA project, *Fusion Eng. Des.* **96–97**, 117 (2015).
- [32] S. Halfon, A. Arenshtam, D. Kijel *et al.*, High-power liquid-lithium jet target for neutron production, *Rev. Sci. Instrum.* **84**, 123507 (2013).
- [33] J. A. Nolen, C. B. Reed, A. Hassanein, V. J. Novick, P. Plotkin, and J. R. Specht, Development of windowless liquid lithium targets for fragmentation and fission of 400-kW uranium beams, *Nucl. Instrum. Methods Phys. Res., Sect. B* **204**, 293 (2003).
- [34] T. Kanemura, M. LaVere, R. Madendorp, F. Marti, T. Maruta, Y. Momozaki, P. N. Ostroumov, A. S. Plastun, J. Wei, and Q. Zhao, Experimental demonstration of the thin-film liquid-metal jet as a charge stripper, *Phys. Rev. Lett.* **128**, 212301 (2022).
- [35] Y. Momozaki, J. Nolen, C. Reed *et al.*, Development of a liquid lithium thin film for use as a heavy ion beam stripper, *J. Instrum.* **4**, P04005 (2009).
- [36] S. G. Durbin, M. Yoda, S. I. Abdel-Khalik, and D. L. Sadowski, Turbulent liquid sheets for protecting IFE reactor chamber first walls, *Fusion Sci. Technol.* **44**, 307 (2003).
- [37] J. A. Nolen, C. B. Reed, V. J. Novick, J. R. Specht, J. M. Bogaty, P. Plotkin, and Y. Momozaki, Behavior of liquid lithium jet irradiated by 1 MeV electron beams up to 20 kW, *Rev. Sci. Instrum.* **76**, 073501 (2005).
- [38] S. G. Durbin, T. P. Koehler, J. J. R. Reperant, M. Yoda, S. I. Abdel-Khalik, and D. L. Sadowski, Surface fluctuation analysis for turbulent liquid sheets, *Fusion Sci. Technol.* **45**, 1 (2004).
- [39] S. G. Durbin, M. Yoda, S. I. Abdel-Khalik, Flow conditioning design in thick liquid protection, *Fusion Sci. Technol.* **47**(3), 724 (2005).
- [40] F. Berg, L. Desorgher, A. Fuchs *et al.*, Target studies for surface muon production, *Phys. Rev. Accel. Beams* **19**, 024701 (2016).
- [41] A. Hassenein, S. A. Kahn, B. J. King *et al.*, The primary target facility for a neutrino factory based on muon beams, in *Proceedings of the 19th Particle Accelerator Conference, Chicago, IL, 2001* (IEEE, Piscataway, NJ, 2001), p. 1583.
- [42] X. Ding, D. Cline, H. Kirk *et al.*, A pion production and capture system for a 4 MW target, in *Proceedings of the International Particle Accelerator Conference, Kyoto, Japan, 2010* (ICR, Kyoto, Japan, 2010), p. 4272.
- [43] M. Paul, A. Arenshtam, S. Halfon *et al.*, A high-power liquid-lithium target (LiLiT) for neutron production, *J. Radioanal. Nucl. Chem.* **305**, 783 (2015).
- [44] C. Ahdida, D. Bozzato, D. Calzolari *et al.*, New capabilities of the fluka multi-purpose code, *Front. Phys.* **9**, 705 (2022).
- [45] J. F. Crawford, M. Daum, G. H. Eaton *et al.*, Measurement of cross sections and asymmetry parameters for the production of charged pions from various nuclei by 585-MeV protons, *Phys. Rev. C* **22**, 1184 (1980).
- [46] J. F. Crawford, M. Daum, G. H. Eaton *et al.*, Production of low energy pions by 590 MeV protons in nuclei, *Helv. Phys. Acta* **53**, 497 (1980).
- [47] K. Nakamura (Particle Data Group), Review of particle physics, *J. Phys. G* **37**, 075021 (2010).
- [48] R. Frosch, J. Löffler, and C. Wigger, Paul Scherrer Institute Technical Report No. TM-11-92-01, 1992.
- [49] R. L. Burman and E. S. Smith, Parametrization of pion production and reaction cross sections at LAMPF energies, Los Alamos National Laboratory Technical Report No. LA-11502-MS, 1989.
- [50] D. R. F. Cochran, P. N. Dean, P. A. M. Gram, E. A. Knapp, E. R. Martin, D. E. Nagle, R. B. Perkins, W. J. Shlaer, H. A. Thiessen, and E. D. Theriot, Production of charged pions by 730-MeV protons from hydrogen and selected nuclei, *Phys. Rev. D* **6**, 3085 (1972).
- [51] P. Denes, B. D. Dieterle, D. M. Wolfe, T. Bowles, T. Dombeck, J. E. Simmons, T. S. Bhatia, G. Glass, and W. B. Tippens, Production of positive pions by 800 MeV protons on carbon, *Phys. Rev. C* **27**, 1339 (1983).
- [52] R. Eichler, D. Kiselev, A. Koschik *et al.*, IMPACT conceptual design report, Paul Scherrer Institut, PSI Bericht, Report No. 22-01, 2022.
- [53] J. J. Back, C. Densham, R. Edgecock, and G. Prior, Particle production and energy deposition studies for the neutrino factory target station, *Phys. Rev. ST Accel. Beams* **16**, 021001 (2013).

- 
- [54] V. Graves, H. Kirk, H. Park *et al.*, Systems testing of a free HG jet system for use in a highpower target experiment, in *Proceedings of the 22nd Particle Accelerator Conference, PAC-2007, Albuquerque, NM* (IEEE, Piscataway, NJ, 2007), p. 3136.
- [55] K. T. McDonald, H. G. Kirk, H. Park *et al.*, The merit high-power target experiment at the CERN PS, in *Proceedings of the 23rd Particle Accelerator Conference, Vancouver, Canada, 2009* (IEEE, Piscataway, NJ, 2009), p. 795.